Cement and Concrete Research

Microstructural analysis of plain and reinforced mortars under chloride-induced deterioration

D.A. Koleva [a,*], J. Hu [a], A.L.A. Fraaij [a], K. van Breugel [a], J.H.W. de Wit [b]

[a] *Delft University of Technology, Department Civil Engineering and Geosciences, Section Material Science, 2628 CN Delft, The Netherlands*
[b] *Delft University of Technology, Faculty of Materials Science and Engineering, Corrosion Technology and Electrochemistry Department, Mekelweg 2, 2628 CD Delft, The Netherlands*

Abstract

This paper reports the results of microstructural analysis of plain and steel-reinforced mortar specimens deteriorated by chlorides that were admixed or introduced through chloride ingress. The electrical properties of mortars were measured and their microstructural characteristics were investigated using quantitative image analysis techniques. The influence of chloride ions on mortar microstructure are discussed in terms of hydration and corrosion products. The research reveals that chlorides will induce changes in the chemical compositions and morphology of cement hydration products, and thereby exert influence on ion transport in the mortar specimens. The electrical properties of plain and reinforced mortars are not only related to the presence of chlorides in the pore system but are also influenced by the pore structure characteristics. The cementitious matrix undergoes certain alterations in conditions of the combined effects of: cement hydration, chloride ion transport and chemical binding mechanisms. To this end the pore structure characteristics appeared to be a significantly contributing factor in the process of chloride-induced corrosion in reinforced cement-based materials.
© 2006 Elsevier Ltd. All rights reserved.

1. Introduction

The corrosion resistance of concrete structures is of utmost importance in salt bearing environments such as in marine or coastal areas. Large numbers of reinforced concrete structures built in these areas require protection from corrosion. The corrosion of reinforcing steel in concrete is an electrochemical process, which can be quantitatively described in a simplified way by equivalent electrical circuits, from which the polarization resistance (R_p) of the steel surface can be derived. This allows estimation of corrosion current (I_{corr}) and corrosion rate (CR, generally expressed in µm/year). It is expected that the corrosion current and consequently the corrosion rate are inversely proportional to the electrical resistance of concrete. The polarization resistance of the steel surface representing the resistance to current flow across the steel–mortar interface at a corrosion potential, is dependent on the formation of passive film of iron hydroxides/oxides during the process of corrosion and is expected to decrease if this protective film is broken under certain conditions.

It is well known that concrete, surrounding steel reinforcement, provides a physical and chemical barrier, thus protecting the reinforcement from corrosion. However, as the structure ages during service life and under certain environmental exposure conditions, corrosion of the reinforcement can still occur, which may lead to deterioration of the concrete structure. Chloride ion is one of the deleterious agents which may cause or promote corrosion. Under marine conditions, chloride ions first react with the $Ca(OH)_2$, reducing the alkalinity of the micro-environment surrounding the reinforcement. Glasser [1] pointed out that the pH is established by the equilibrium between $Ca(OH)_2$, C–S–H, and the pore solution. Penetration of chloride ions into reinforced concrete of relatively high permeability and absorptivity can destroy the protective oxide film which is stable in the alkaline (pH = 12.5–13.5) environment around the

* Corresponding author. Delft University of Technology, CiTG, Material Science, Stevinweg 1, 2628CN Delft, The Netherlands. Tel.: +31 15 278 7451; fax: +31 15 278 8162.
  E-mail address: D.A.Koleva@tudelft.nl (D.A. Koleva).

steel rebar. This induces corrosion of steel, expansion in volume due to corrosion products and subsequent cracking and spalling of concrete surrounding the reinforcement. Some SEM studies conducted on corroded paste–rebar interface have shown that the reaction products consist of iron oxides and oxychloride complexes. A basic iron chloride $3Fe(OH)_2 \cdot FeCl_2$ is formed which later decomposes to produce akaganeite and FeOOH [2]. The corrosion process involves three main phases: depassivation, propagation and final stage (critical time) [3]. Depassivation is the loss of oxide layer during the initiation period, t_p. The propagation phase starts from the completion of depassivation to the final stage at which corrosion during the period, t_{corr} produces spalling and cracking of the concrete. So the service life of reinforced concrete structures can be equated to the critical time, $t_{cr} = t_p + t_{corr}$.

Generally, the corrosion process in reinforced cement-based materials occurs only when a sufficient amount of aggressive substances (e.g. chlorides, sulphates, CO_2 penetration) are present at the steel/cement paste interface at certain threshold values [4]. The corrosion initiation will depend on the rate of penetration of aggressive substances from the environment into the cement-based bulk matrix i.e. it will depend on the electrolytic paths in the system. The electrolytic path, along with the moisture and oxygen content, will determine the ease of ion transport through the bulk matrix to the steel/paste interface. Consequently, the transport properties will depend on the microstructural characteristics of the bulk cementitious materials i.e. porosity, pore interconnectivity, pore size distribution. Electrical resistivity of cement-based materials is one of the parameters strongly influencing ion transport. Electrical resistivity is determined by the moisture content but also depends on the bulk material microstructure along with the pore water composition.

Available are a number of techniques for concrete repair and rehabilitation with varied success. Among the most successfully applied techniques are the electrochemical methods of repair i.e. desalination, re-alkalization, cathodic protection. As the corrosion process (as well as the efficiency of the electrochemical protection techniques) depends, among other factors, on the electrical resistivity of the bulk matrix and the electrochemical parameters of the steel reinforcement, the purpose of this preliminary study was to investigate the influence of chloride ions on the microstructure and on electrical properties of plain and reinforced mortars. This paper specifically examines chloride-induced changes in the morphology of hydration products, pore structure of plain and reinforced mortars, chemical composition of C–S–H products and corrosion products at the steel/mortar interface. Structural information of the steel/mortar interfacial zone and of the bulk mortar can be obtained from backscattered electron (BSE) images with the aid of quantitative image analysis. This allows quantitative characterization of microstructural modifications due to accelerated hydration in the presence of admixed chlorides and due to chloride-induced reinforcement corrosion. The reinforcement steel parameters were determined using Linear Polarization Resistance (LPR) and Electrochemical Impedance Spectroscopy (EIS). A combination of electrochemical measurements with microstructural analysis of the mortar specimens leads to better understanding of the electrochemical processes that occur during corrosion. Such analysis captures the relevant modifications associated with the evolving transport and durability properties of reinforced cementitious systems subject to chloride-induced deterioration.

2. Experimental

2.1. Sample preparation of plain and reinforced mortars

Plain mortar prisms of $40 \times 40 \times 160$ mm and reinforced mortar cylinders of 40 mm in diameter and 100 mm height were cast according to standard experimental procedures, using ordinary Portland cement CEM I 32.5R, cement to sand proportions of 1:3 and water to cement ratio of 0.5 for the prisms and 0.6 for the cylinders. Details of the specimens' set-up, curing conditions and mortar mixtures are given in Table 1; the chemical composition, physical characteristics and constituents of the used cement are given in Table 2.
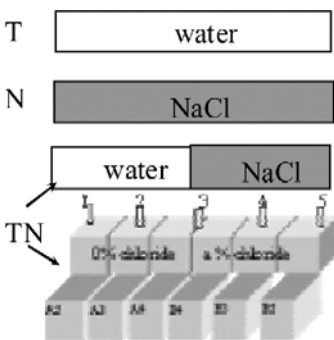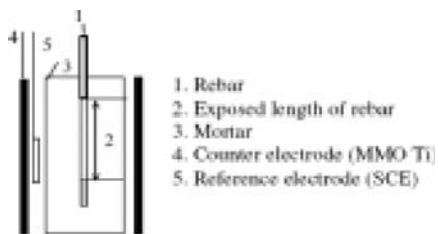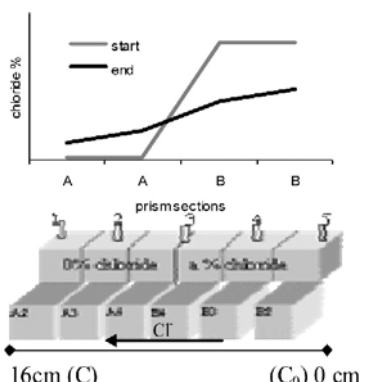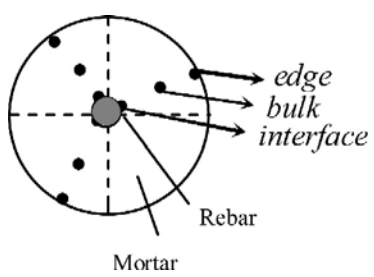
As seen from Table 1, the group of plain mortar prisms (15 specimens in total) comprised three sub-groups of specimens, varying in chemical compositions of the mixing solutions i.e. group *T* made with tap water, group *N* produced using 3% NaCl solution as mixing water and group TN, a half to half combination of the mixture for *T* and for *N* specimens (Table 1, point 1). The specimens were stored in a fog room maintained at 20 °C and 98% relative humidity (RH) during the whole period of 65 days of testing. Stainless steel pins were equidistantly embedded along specimen length, each pin being embedded to a depth of 30 mm into the specimen for the purpose of resistivity monitoring.

The group of reinforced mortar cylinders (12 specimens in total) were cast using the same cement, sand and same mixing procedures as for the plain mortars (Table 1, point 4). Each cylinder contained a centrally located 6 mm diameter steel bar (using "as received" FeB500HKN construction steel) with exposed length of 80 mm (Table 1, point 1). All specimens were cured in the fog room conditions of 98% RH and 20 °C for 14 days and then placed in lab air, 20 °C and certain experimental conditions (Table 1, point 3) till the end of the testing period of 120 days. The reinforced cylinders comprised two experimental groups: reference (non-corroding) specimens denoted as *R* and corrosion test samples denoted as *N* (Table 1, point 2). A cylindrical titanium mesh served as counter electrode and saturated calomel electrode (SCE) was used as reference electrode for the electrochemical measurements [5].

2.2. Resistivity measurements of plain mortars

Resistance monitoring was conducted on specific sections of the prism specimens (Table 1, point 1) to provide insight into ion concentrations gradient due to diffusion. Measurements of the total resistance gave information on the changes in electrical properties of specimens under various chloride ion concentrations and under various chloride concentration gradients. Resistance measurements were performed using direct

Table 1
Specification of materials set-up, conditioning and some experimental procedures

	Plain mortar prisms	Reinforced mortar cylinders
1. Specimen set-up		
		1. Rebar
		2. Exposed length of rebar
		3. Mortar
		4. Counter electrode (MMO Ti)
		5. Reference electrode (SCE)
2. Specimen groups	– Dimensions $40 \times 40 \times 160$ mm	– Dimensions $d=40$ mm, $h=100$ mm
	– T — using tap water as mixing water	– R — reference
	– N — using 3% NaCl solution as mixing water	– N — corroding
	– TN — half-to-half the mixture of T and N	All specimens cast with demi-water
3. Curing conditions	– 60 days — fog room (98% RH, 20 °C)	– 14 days fog room (98% RH, 20 °C)
		– 106 days lab air, 20 °C in immersed conditions:
		R — 1/3rd of height immersed in water
		N — 1/3rd of height immersed in 7% NaCl solution
4. Mortar mixture (see also Table 2)	– OPC CEM I 32.5 R	– OPC CEM I 32.5 R
	– W/C ratio 0.5, cement to sand ratio 1:3	– W/C ratio 0.6, cement to sand ratio 1:3
	– Sand of size range 125 µm to 2 mm	– Sand of size range 125 µm to 2 mm
	– Preparation EN 196-1	– Preparation EN 196-1
	– Embedded into 30 mm depth stainless steel pins for resistivity measurements	– FeB500HKN, $d=6$ mm as embedded re-bar, exposed length 80 mm
5. Chloride profile		5a. Areas for pore structure analysis
	Chloride concentrations determined wet chemically by sections of the prisms TN	
6. Resistivity measurement	Using 2 and 4 pin AC methods and the embedded pins.	Using EIS measurements (set-up p.1) and the system response at highest frequency.

current (DC) four pin method, and the alternating current (AC) two and four pin methods. For the DC measurement, a DC current of 2 mA was applied to the outer pins 1 and 5 according to the scheme shown in Table 1, then the voltage drop in every section was recorded. For the AC measurement, a specially designed device referred to as R-meter was used. By applying alternating current of 1 mA at a frequency of 1 kHz, the device outputs a DC voltage, which represents the actual resistance. It was found that the different methods yielded similar outcomes with a coefficient of variation within 3 to 5%. Electrical resistivity was calculated from recorded resistance values using the equation: $\rho = RA/l$, where ρ is the resistivity in Ω m, R is

the resistance in Ω, A is the cross-section in m^2, and l is the length in m.

2.3. Chemical analysis

Wet chemical analysis for determination of ion concentrations was performed for the plain concrete prisms according ASTMC1218 and ASTMC1152 for free and total chloride concentrations, using Volhard titration method. An Inductive Coupled Plasma Spectrometer (ICP-AES) was used for determination of alkali concentrations. The chemical analysis was performed for each section of the plain mortar prisms

Table 2
Chemical properties, physical properties and constituents of CEM I 32.5 R (ENCI)

Chemical		Constituents		Physical strength of standard mortar	
Oxide	Weight(%)	Phases*	Weight(%)		
CaO	63.90	C_3S	63	2 days	22 MPa
SiO_2	21.00	C_2S	13	7 days	36 MPa
Al_2O_3	5.03	C_3A	8	28 days	49 MPa
SO_3	3.00	C_4AF	9	Blaine	285 m^2/kg
Fe_2O_3	2.83				
MgO	2.00				
Na_2O	0.24				
K_2O	0.65				
TiO_2	0.30				
P_2O_5	0.16				
Mn_2O_3	0.06				
total	99.17				

*C_3S — tricalcium silicate; C_2S — dicalcium silicate; C_3A — tricalcium aluminate; C_4AF — ferrite.

(Table 1, point 1) at 1, 8, 14, 24, 30, 41 and 57 days of cement hydration. The chemical analysis aimed at monitoring ion transport due to diffusion (as result of concentration gradient) in sub-group TN for the plain mortar prisms and compare changes in concentration with sub-groups *T* and *N* (no concentration gradient). Consequently a chloride profile can be derived at the end of the test for specimens sub-group TN, using the second Fick's law and the arrangement schematically shown in Table 1, point 5. The derived changes in chloride and alkali concentra-

tions (due to concentration gradient) were further coupled with electrical resistivity measurements for the same sections of the prisms (Table 1. points 1 and 5), thus giving a correlation of ion transport and electrical properties in the bulk mortar matrix with aging and in the present conditions.

2.4. Electrochemical measurements on reinforced mortars

The electrochemical behaviour of steel reinforcement in the mortar cylinders (Table 1) was investigated using LPR and EIS methods. The parameters used to characterize the corrosion behaviour of reinforced mortars include the corrosion potential (E_{corr}), the corrosion current density (I_{corr}), obtained from R_p values and the electrical resistivity of the mortar. The electrochemical measurements were performed at open circuit potential (OCP) for all cells and in immersed condition (7% NaCl for groups *N* and water for group *R*) using SCE as reference electrode. For LPR an external polarization in the range of ±20 mV vs OCP was used at scan rate 0.16 mV/s. The EIS measurements were carried out in the frequency range of 50.5 kHz to 10 mHz by superimposing an AC voltage of 10 mV. The used equipment was EcoChemie Autolab (Potentiostat PGSTAT30), combined with FRA2 module, using GPES and FRA [5].

The corrosion rate (CR) can be directly estimated from R_p values, derived either from LPR or EIS measurements. In addition to electrochemical characteristics of the steel surface, the EIS approach provides insight into the electrical properties of the mortar matrix by recording the system impedance
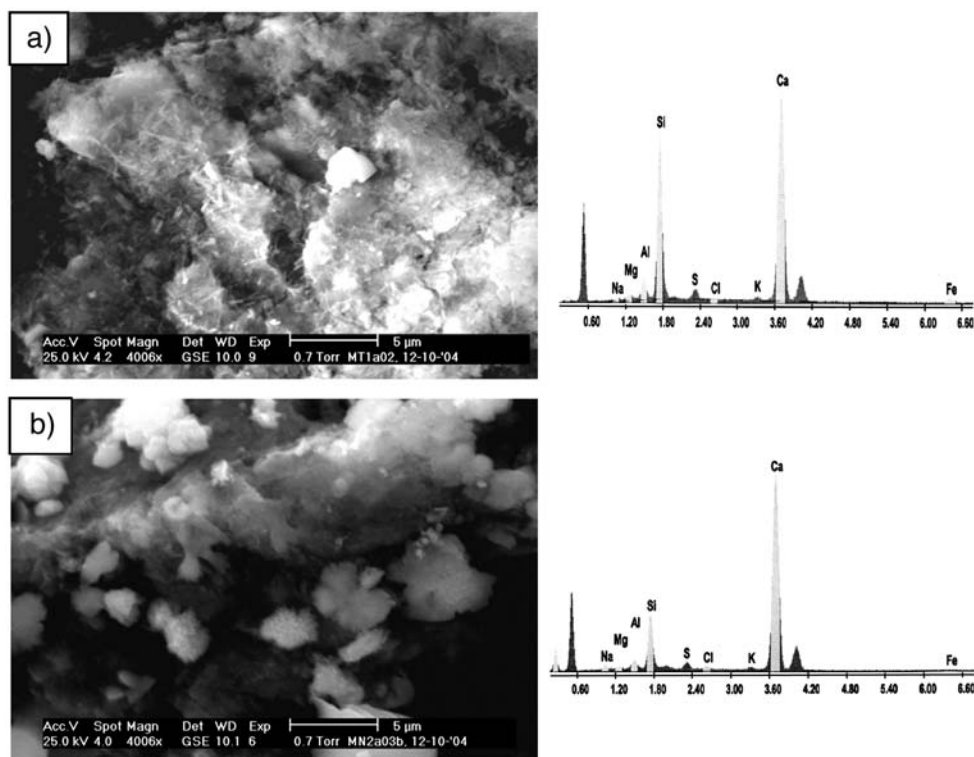

Fig. 1. SEM images and the corresponding EDX spectrums of plain mortars: a) without admixed chlorides (sample *T*) and b) with admixed chlorides (sample *N*).
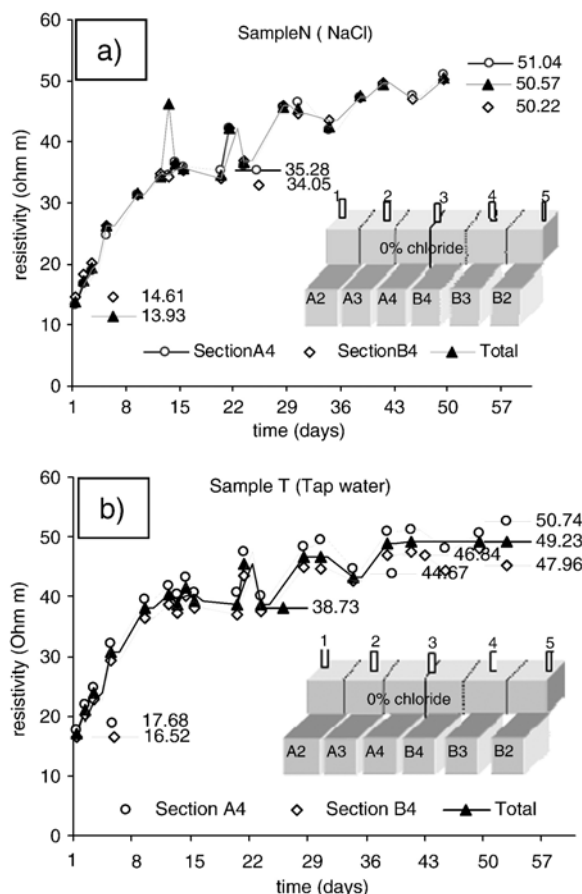
Fig. 2. Resistivity measurements of the plain mortars: a) N specimen, b) T specimen during the first two months of hydration. The measurements are taken at different sections and as total of the prism (Table 1, p.1, 5).

response at the highest frequency employed. The electrical properties of the steel/mortar interface and the corrosion process are generally characterized in terms of an equivalent circuit, consisting of combination of resistances and capacitors [6–8].

2.5. SEM imaging and EDX analysis

A set of BSE images were taken at randomly selected locations on the polished sections of the plain mortar prisms and in radial direction of increasing distance from the steel surface in the reinforced mortar cylinders (Table 1, point 5a). The size of the reference region of each image is 226 μm in length and 154 μm in width, with a resolution of 0.317 μm/pixel (500×). Small capillary pores play an important role in the transport properties of cement specimens. Therefore, it is necessary to find a balance between the representative area revealing sufficiently large amount of pores, and a satisfactory resolution for detection of small capillary pores. Hu and Stroeven [9] studied the influence of image resolution on the characterization results of pore structure, and reported that resolutions of 0.293 μm/pixel (1000×) and 0.146 μm/pixel (2000×) gave similar values, although the higher magnification could be expected to reveal more trivial and subtle changes in the pore structure.

Morphological changes in hydration products and corrosion products were observed in SEM images but at much higher

magnifications in the range of 2000 to 4000×. At the same time, EDX analysis and multi-element mapping were employed at specific positions of the image in order to analyze the chemical compositions and spatial distribution of hydration or corrosion products in the plain and reinforced mortars. The equipment used for imaging and microstructural investigation was environmental SEM (ESEM Philips XL30, equipped with EDX detector).

2.6. Pore structure analysis

The original BSE image is segmented by applying a gray-level threshold to create a binary image reflecting the pore phase. The threshold gray level between porosity and solid phases is selected by a technique based on the shape of the histogram of BSE image. The anhydrous material and calcium hydroxide (CH) have fairly uniform gray levels, resulting in sharp peaks in the histograms. Due to variation in composition, the gray levels of the other hydration products (basically C–S–H) form a shallower but still clearly identifiable peak in the histograms. It has been found that consistent results can be obtained by selecting an arbitrary point on the lower slope of the peak produced by the other hydration products [10]. The binary image is then subjected to quantitative image analysis for derivation of structural parameters.
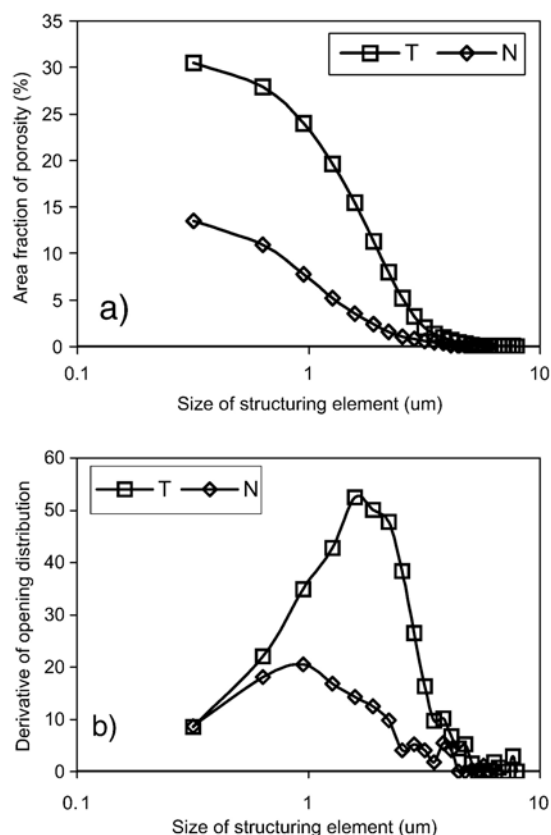

Fig. 3. Opening distribution curves for the two groups of plain mortars a). The critical pore sizes are determined from the peak point on derivatives of opening distribution curves b).
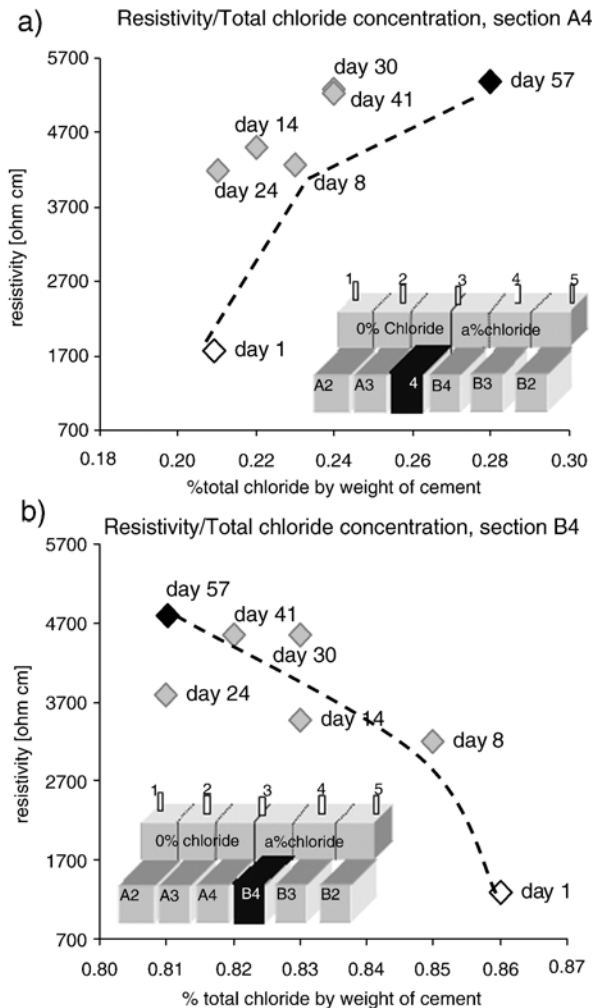
Fig. 4. Correlation of mortar electrical resistivity and total chloride concentration for sections A4 a) and B4 b) of plain mortar prisms TN with hydration time.

Combination of SEM images and quantitative image analysis allows determination of structural information of pore space, such as the porosity and critical pore size. Using a mathematical representation of morphology transformations, pore size distribution can be obtained by applying a sequence of similarly shaped structuring elements of increasing size [11]. The so called "opening distribution" was used in this study. It involves opening of the binary image by a series of squares of increasing size. The "opening distribution" curve of pore space is obtained by plotting the pore area fraction after an opening operation against the linear dimension of the structuring element. This gives a type of "size" classification in the case of an interconnected structure, in contrast to single features. This measurement is a two-dimensional analogy of the type of size distribution obtained by gas or methanol absorption or by low temperature calorimetry.

The definition of critical pore size can be found in the literature [9,12]. The critical pore size, l_c can be conceived as the diameter of the pore that completes the first interconnected pore pathway in a network. Critical pore size is determined using a procedure of sequentially adding pores of diminishing size to the network. It is generally accepted that the smaller the

critical pore size, the finer the pore structure. The critical pore size is a unique transport length scale of major significance for permeability properties. Katz and Thompson [12] supported the conjecture that mercury injection has a percolation geometry and considered the characteristic length, l_c as corresponding to the percolation threshold. This feature can be experimentally assessed by mercury intrusion porosimetry (MIP). A typical mercury injection curve, reflecting the volume percentage of mercury intruded as a function of the applied pressure, is S-shaped. The critical pore size, l_c is associated with the inflection point of the cumulative pore size distribution curve. Similarly, opening distribution method gives a cumulative pore size distribution curve. With this method, the point of inflection is the peak of the derivative of the opening distribution curve [9].

3. Results and discussion

Representative SEM images are given in Fig. 1 for plain mortars, and Figs. 5–8 for the reinforced mortars respectively. The micrographs clearly reveal the differences in porosity and morphology of hydration products induced by chloride ions.

3.1. Chloride-induced changes of hydration products in plain mortars

Fig. 2 shows that the results of resistivity measurements for the plain mortars of T-series and N-series were similar. Fig. 1
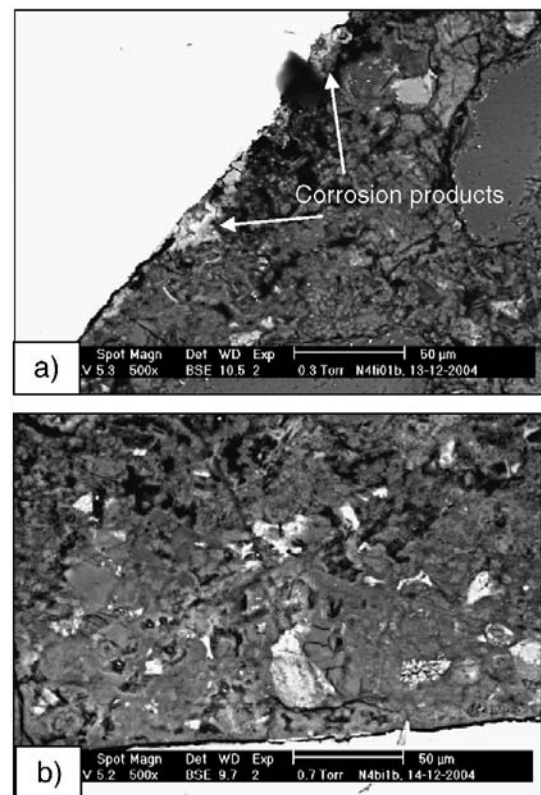

Fig. 5. BSE images of the steel/mortar interface in reinforced mortar N (under chloride ingress). The section images are taken at: a) the upper part (exposed in air) and b) lower part (immersed in NaCl solution) of the specimen. The bright white regions represent steel bar.

presents the typical SEM images and the corresponding EDX spectra for hydrated cement, indicating variations in chemical compositions and morphology of C–S–H in the plain mortar specimens.

The high Ca/Si ratio of at least 2.19 found for the *N* specimens was a chloride-induced effect. The typical Ca/Si ratio of C–S–H in Portland cements is about 1.8. The surface charge on C–S–H depends on its Ca/Si ratio: when the Ca/Si ratio is high, the surface charge of C–S–H is positive and anions such as Cl^- and OH^- are adsorbed on the C–S–H fibers but cations especially Na^+ and K^+ remain in the pore solution. In contrast, if the Ca/Si ratio is lower than about 1.2 to l.3, the surface charge of C–S–H becomes negative and alkali cations are incorporated on the C–S–H, thus decreasing the alkali ion concentrations in the pore solution [13]. Therefore, in the case of relatively high Ca/Si ratio such as 2.19 to 2.95 obtained for the *N* specimens, the alkali ions in the pore solution may not be suppressed by C–S–H as in the case of *T* specimen which had a low Ca/Si ratio of 1.4. Although the porosity values for the *N* samples were significantly lower than for the *T* samples as seen in Fig. 3, similar values of resistivity measurements for the two groups of plain mortars were obtained (see Fig. 2).

The negative charge of the C–S–H in specimens *T* (i.e. increased OH^- concentration in the pore solution) and the positive charge of C–S–H in specimens *N* (i.e. OH^- and Cl^- adsorbed on the C–S–H fibers, thus a decreased amount of OH^- and Cl^- will be present in the pore solution), is probably one of
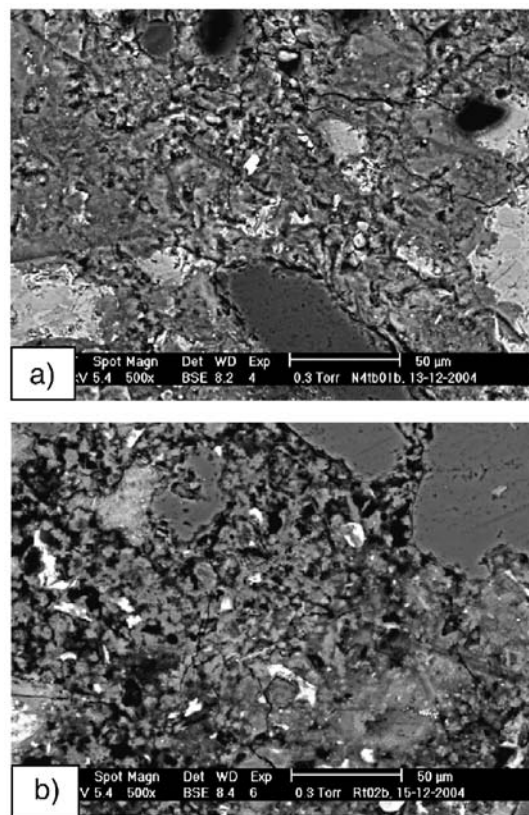

Fig. 7. BSE images of bulk cement paste in: a) corroding *N* and b) reference *R* mortars.
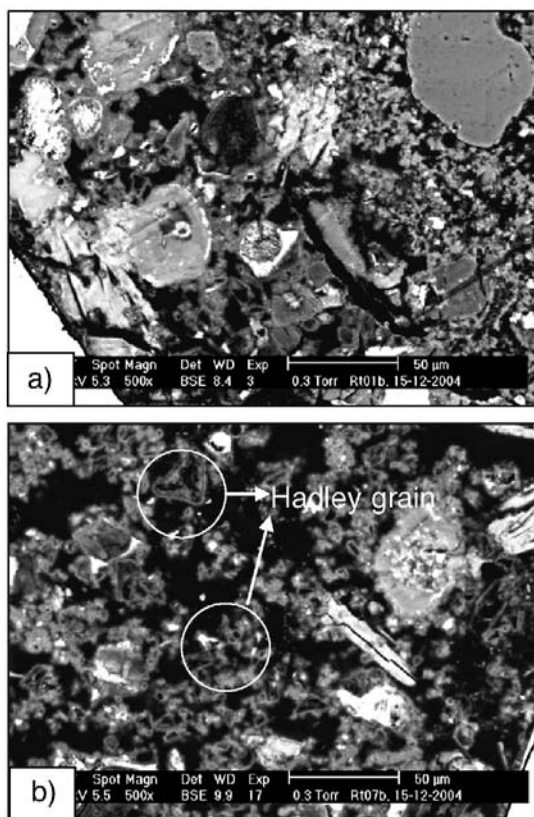

Fig. 6. BSE images of the reference reinforced mortar *R* (without external chloride ingress) at different locations on the steel/mortar interface.

the reasons for similar electrical resistivity values for specimens *T* and *N*. Further, if a correlation of derived chloride concentrations and electrical resistivity values is performed (Fig. 4), it is obvious that microstructural alterations and surface charge of the bulk matrix are factors, significantly contributing to the electrical properties, rather than the conductive nature of chloride ions alone. As seen from Fig. 4, chloride concentration increases in section A4 (Fig. 4a)) and decreases in section B4 (Fig. 4b)) (as already mentioned chloride diffusion due to concentration gradient is in direction from sections B (cast with 3% NaCl) towards sections A (initially free of chlorides) in the specimens TN, Table 1). Electrical resistivity values however are similar by sections (as also shown on Fig. 2), moreover electrical resistivity increases in both sections A4 and B4 with time, despite the differences in chloride concentration. The phenomenon is a combined effect of cement hydration with aging on one hand, the influence of NaCl as accelerator of cement hydration on the other [14,15] and the alterations in microstructural properties of the bulk matrix. As reported in [16], bulk conductivity measurements and their respective pore fluids in comparable mortar mixtures, even if no chlorides are present in the cementitious matrix, show that changes in pore structure exert a greater influence on the measured conductivity i.e. the electrical properties at early ages of hydration are determined mainly by changes in the pore structure, rather than changes in the pore solution. Hence, resistivity is not only dependant on the presence of conductive ions (as chlorides) in the pore solution, but is also a function of
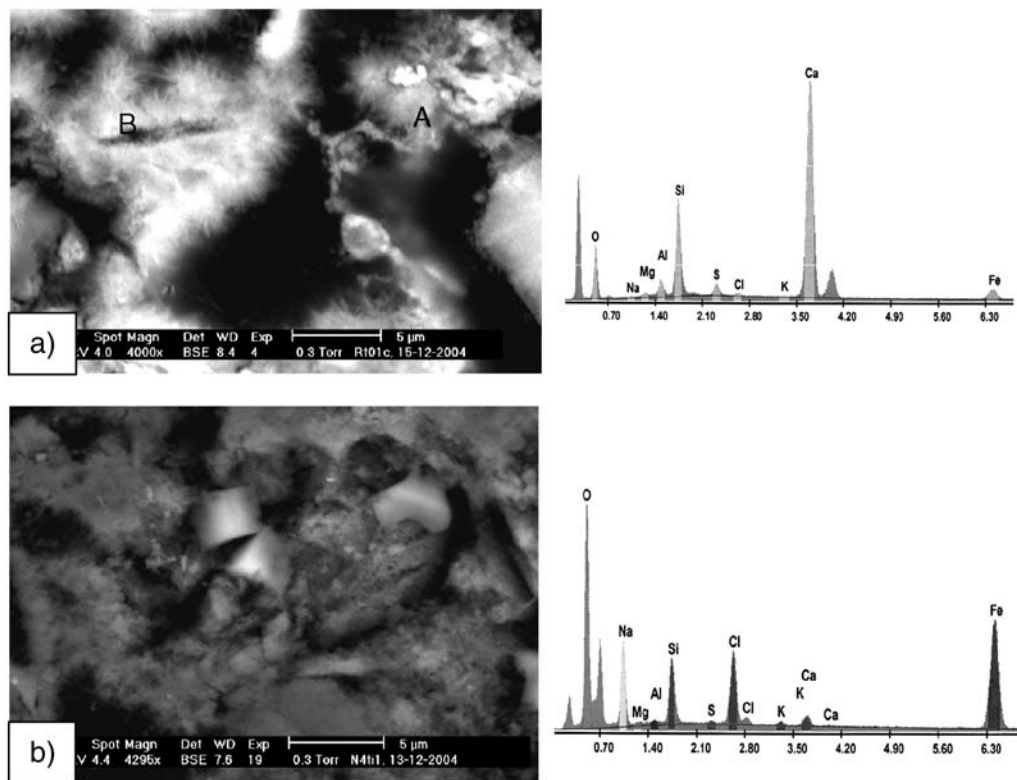
Fig. 8. SEM images and the corresponding EDX spectrums of the microstructure in the vicinity of steel surface in reinforced mortars: a) reference sample R, b) corroding sample N.

the pore structure and the physico-chemical changes in the C–S–H matrix (as discussed above), thus influenced by the movement of the pore solution ions in the pore network.

3.2. Chloride-induced microstructural changes in reinforced mortars

The formation of corrosion products in corroding specimen N and lack thereof in the reference specimen R can be seen in Figs. 5 and 6, while Fig. 7 provides a comparison of bulk mortar microstructure between the corroded and reference specimens. Fig. 5a) shows the steel/mortar interface in the upper part of specimen N, revealing the presence of corrosion products. This is the part of the specimen where the bulk mortar had showed a higher degree of shrinkage cracking due to exposure to air, and cracks appeared to be interconnected through voids as seen in Fig. 7a). It is known that the volume of corrosion products is larger than the volume of the reactants, thus the excessive formation of the products results in expansive pressure causing cracking in hardened cementitious systems. The newly formed cracks tend to connect with other existing cracks forming a percolating network, which in turn promotes further ingress of chloride ions into the mortar.

Hadley grains, the hollow hydrate shells such as seen in Fig. 6b), were evident in the reference mortar. Its thin shells consist of C–S–H. The reasons for this phenomenon are not well understood, but it appears that the aluminate phase has an important influence. The formation of a possibly amorphous

product of C_3A hydration on the surface of the cement grains might inhibit the precipitation of C–S–H on the grain surface and lead to the formation of the separated shells [10]. These are a common feature in all cement pastes. The reference specimen which had a lower hydration rate and a more porous steel/mortar interface than the N specimen showed more Hadley grains.

Fig. 8 presents SEM images and corresponding spectra for the reinforced mortars, revealing the differences in morphology and chemical compositions of hydration products for the reference and the corroding samples. Both images were taken at a distance of 50 μm away from the steel surface. Fig. 8a) indicates the C–S–H (A) and ettringite formation (B) in the reference sample, while Fig. 8b) shows C–S–H intermixed with a cubic crystal of NaCl in the corroding sample.

Elemental mapping was employed for evaluating chemical composition of hydration and corrosion products in the mortar/steel interfacial transition zone, within 100 μm distance away from the reinforcement surface. Fig. 9a) is a SEM image of the interface revealing the existence of corrosion products in sample N and lack thereof in group R (Fig. 9e)). Fig. 9b) and f) indicate the spatial distribution of calcium (Ca) and silica (Si) in the vicinity of the steel bar in specimens N and R respectively. The presence of Si is mainly from aggregates, while Ca is from hydration products. The regions indicated on Fig. 9d) show lack of Ca and Si at the reinforcement/mortar interface where the chloride-induced corrosion products are found. Fig. 9c) is the elemental mapping of the image shown in Fig. 9a) for Al^{3+}, Ca^{2+}, Na^+, Cl^-, suggesting a possible formation of Friedel's salt under
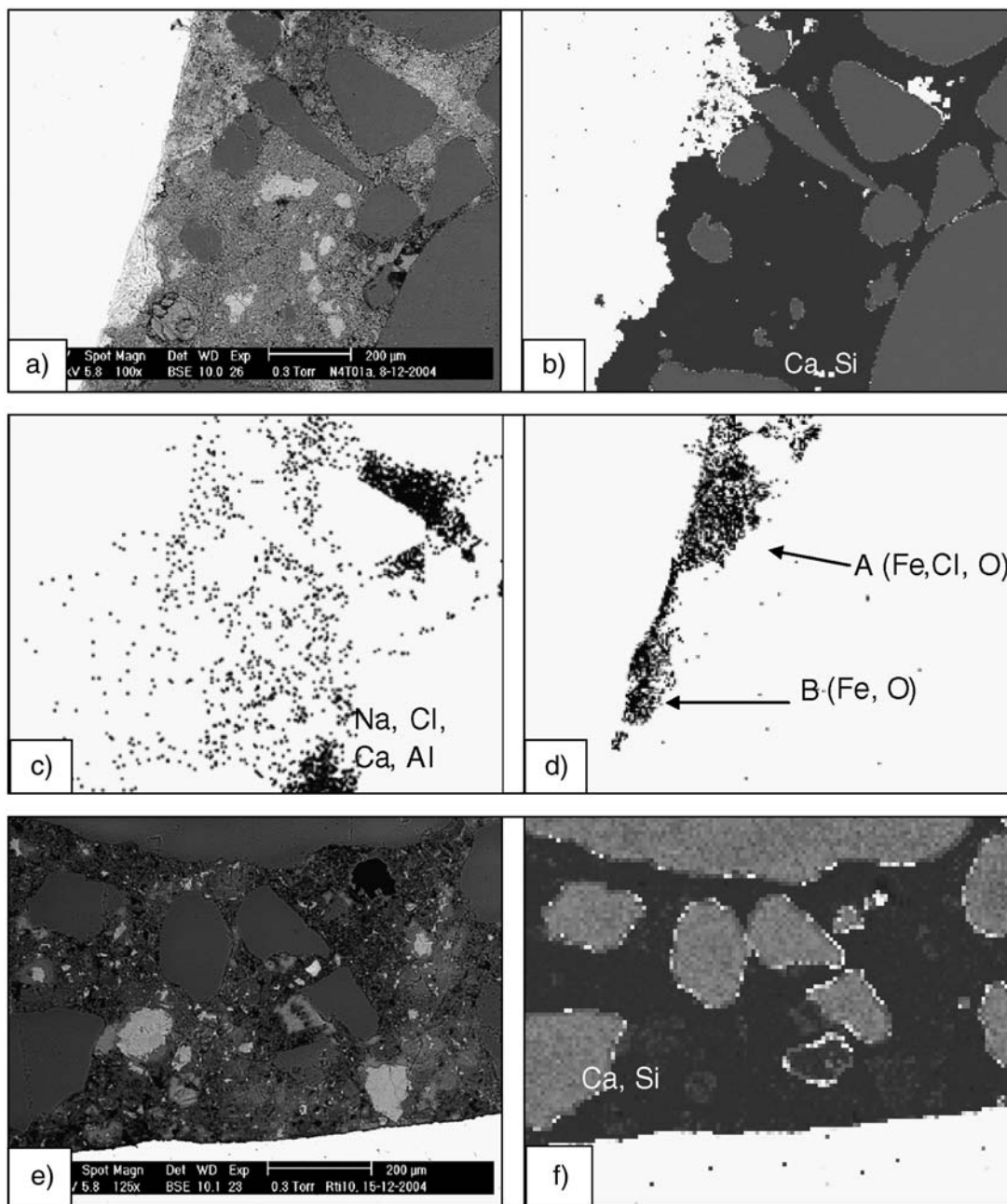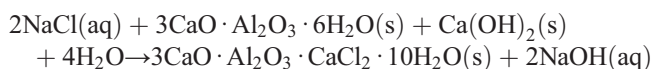
Fig. 9. Elemental mapping, suggesting possible presence and distribution of Friedel's salt c), corrosion products composed of iron oxides and iron oxychloride complexes d).

chloride ingress. It is known that when NaCl comes in contact with free tricalcium aluminate, the following chemical reaction will lead to Friedel's salt formation.

$$2NaCl(aq) + 3CaO \cdot Al_2O_3 \cdot 6H_2O(s) + Ca(OH)_2(s)$$
$$+ 4H_2O \rightarrow 3CaO \cdot Al_2O_3 \cdot CaCl_2 \cdot 10H_2O(s) + 2NaOH(aq)$$

However, Friedel's salt can also form through chloride attack on existing ettringite [17].

Fig. 9d) presents the mapping of elements Fe and O, indicating the presence of iron oxidization products. It should be noted that the upper indicated as A, and lower part indicated as B had significantly different chemical compositions of the corrosion products. In part A of Fig. 9d), element mapping and EDX both indicate a significant amount of chloride, suggesting the presence of iron oxychloride complexes. The corrosion products in part B are mainly composed of Fe and O, with negligible Cl. It suggests that the corrosion products may consist of iron oxides/hydroxides, Fe_2O_3, Fe_3O_4, and $FeOOH$. The portion of FeOOH in corrosion products reportedly increases significantly when the concentration of NaCl solution changes from 0.5% to 1% [18], hence, the content of FeOOH could be relatively high in the region B. In contrast, Fig. 9e) and
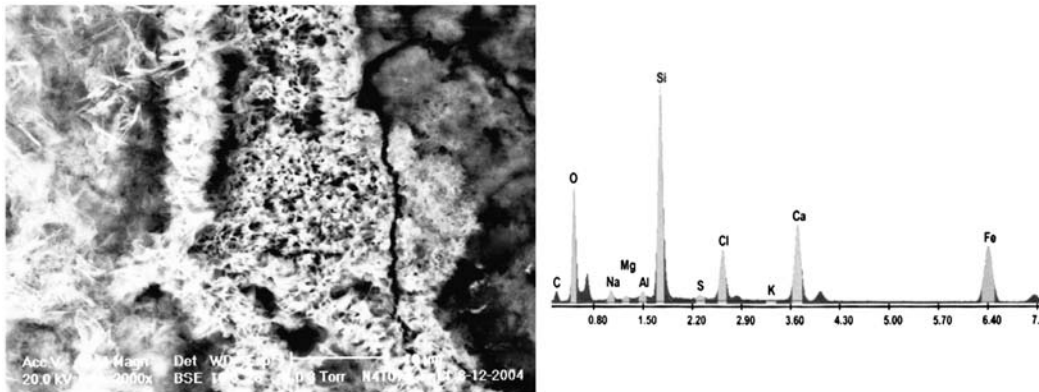
Fig. 10. BSE image and corresponding EDX spectrum of delicate globular and whiskery mineral (iron oxychloride complexes) formed due to rebar corrosion in *N* specimen. The figure is taken at a specific position in region A of Fig. 9d).

f) show the steel/cement paste interface in specimens *R* that were free of corrosion products.

The crystals of oxychloride complexes are generally of lamellar, globular or whiskery shape. It is the lamellar type crystals that are expected to be responsible for volumetric expansion and not the delicate, globular and whiskery minerals. Fig. 10 provides a BSE image showing iron oxychloride complexes and the corresponding EDX spectrum taken at a specific position of the corrosion products in part A of Fig. 9d).

3.3. Microstructural characterization of reinforced mortars

Fig. 11 shows the pore size distribution at the steel/mortar interface in reinforced mortars groups *N* and *R* at the age of 120 days. It is clear that the reference specimen *R*, had a coarser pore structure, characterized by a porosity of 12.68% and critical pore size of 2.8 μm for the top sections and porosity of 8.8% and critical pore size of 1.27 μm for the bottom section of the specimen. The porosity and critical pore size decreased to 10.87% and 1.27 μm respectively, for the top section and to 4.04% and 1.27 μm for the bottom section of the corroding specimen, *N* (Fig. 11). The bottom sections of both specimens, being submerged in NaCl solution for specimen *N* and water for specimen *R*, have lower porosity compared to the relevant top aerated sections, which is due to moist conditions provided by the solutions. The finer pore structure of the bottom section of specimen *N* however, demonstrates that the chloride ions promote cement hydration, evidenced by the much lower porosity of 4.04% in the bottom section of specimen *N*, compared to the porosity of 8.80% in the bottom section of *R* specimen.

Fig. 12 shows the variation of the pore structure of the corroding specimen *N* (Fig. 12 a), b)) and the reference specimen *R* (Fig. 12 c), d)) in the radial direction of increasing distance from the steel surface (schematically presented in Table 1, point 5a).

For both specimens *N* and *R*, the bulk and edge parts of the specimens (both immersed and aerated sections) have similar porosity values and approximate pore size distribution curves. The steel/mortar interface is expected to be more porous in both specimens, characterized by much higher values of porosity and

critical pore size. However, for the bottom section of *N* specimen, the porosity distribution is much more uniform, without an obvious gradient in the radial direction (Fig. 12a)). The
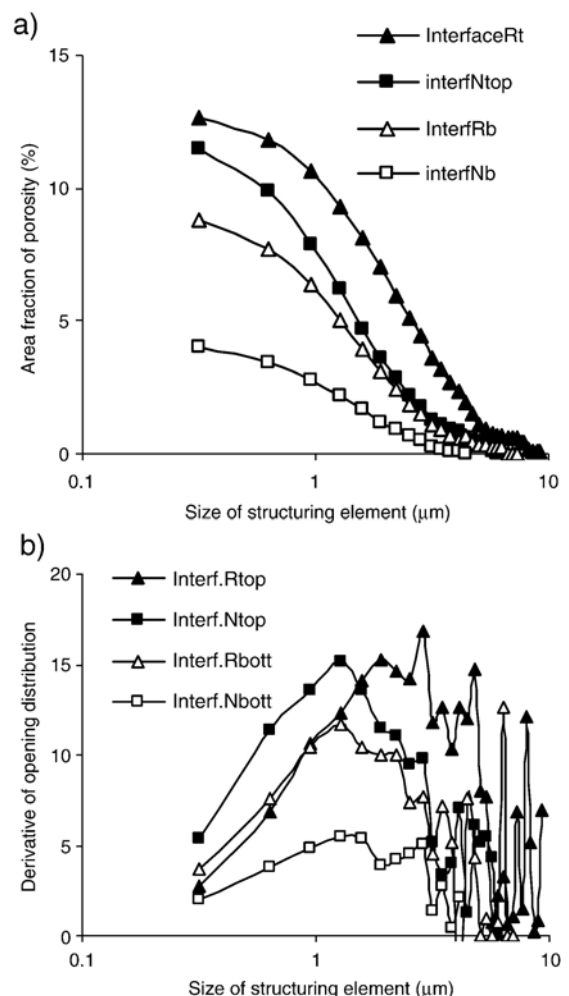

Fig. 11. Pore structure changes in the steel/cement paste interface of reinforced mortars, exposed to chloride ingress (120 days of age); a) pore size distribution; b) critical pore size.
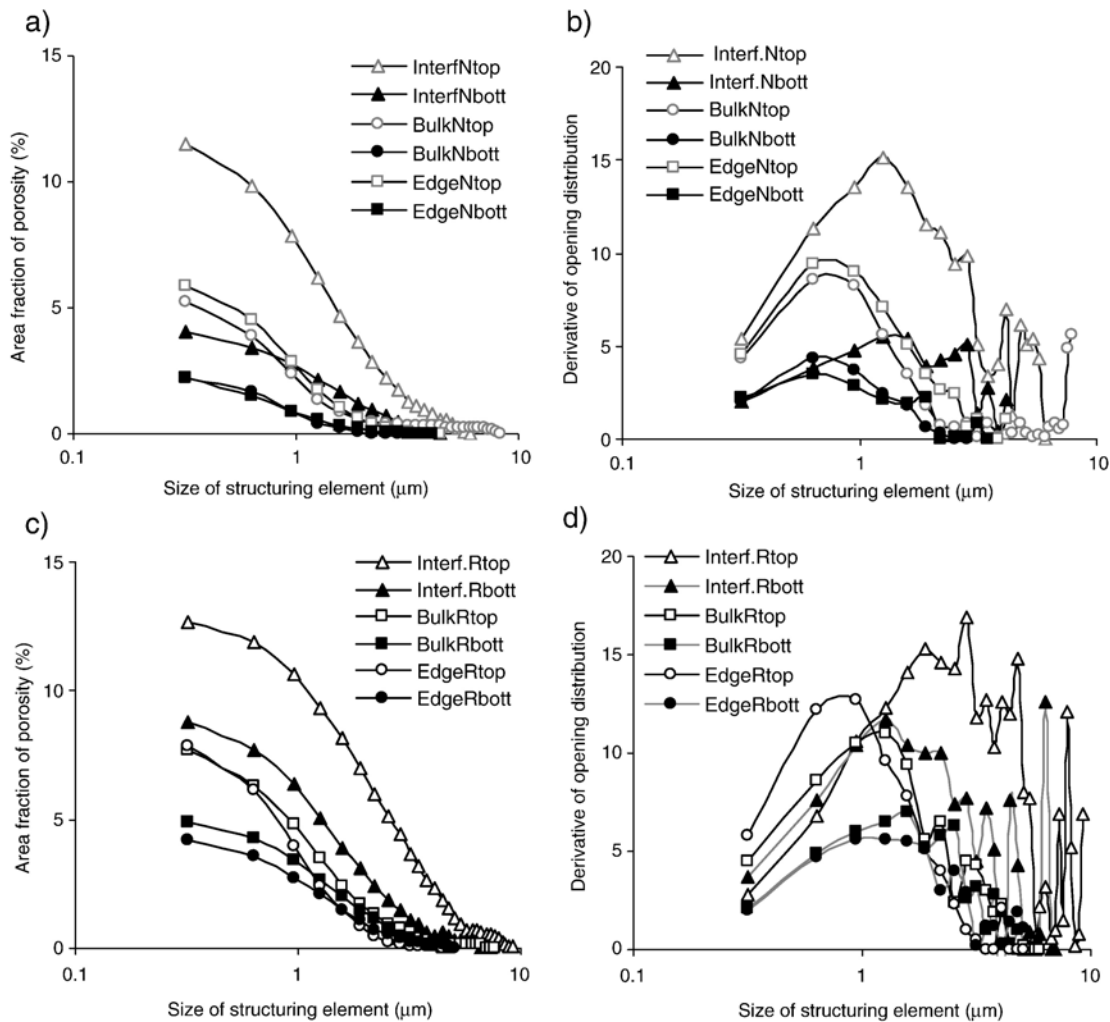
Fig. 12. Pore structure changes in the radial direction of reinforced mortars (120 days of age), exposed to chloride ingress (locations presented in Table 1, p.5a): a) and c) — pore size distribution; b) and d) — critical pore size of specimens N and R respectively.

phenomenon confirms the influence of NaCl in refining the pore network (as also reported in [19,20]) i.e. significantly reducing the porosity and critical pore size of the submerged (bottom) section and also inducing pore refinement in the aerated (top) section of the specimen N, compared to specimen R. The reduction in porosity from top (aerated) section to bottom (immersed) section for specimen R is due to hydration with aging for both sections and the additional moist conditions for the bottom section. The reduction is in the range of: 30% from top to bottom in the interfacial zone; 37% from top to bottom for the bulk and 46% from top to bottom for the edge locations. The reduction in porosity and critical pore size for the corroding specimen N is a result of combined effects of hydration (in both sections), moist conditions for bottom section and the influence of NaCl in both sections (due to capillary suction chlorides can exert influence in the top aerated section as well). Thus, the reduction in porosity in specimen N is far more significant, compared to specimen R and is in the range of: 65% from top to bottom for the interfacial zone, 57% from top to bottom for the bulk and 62% for the edge locations.

4. Influence of microstructure on electrical properties and ion transport

4.1. Permeability prediction for plain mortars

Relevant to the morphological aspect of pore structure the specific surface area, S_V is a widely used parameter. It is defined as the surface area of pore phase per unit test volume in standard

Table 3
Structural information derived from SEM images for plain mortars (w/c ratio 0.5, 65 days of age)

Parameters	T (using tap water)	N (using NaCl)
Porosity (%)	30.46 (11.47%)	13.54 (12.60%)
Critical pore size l_c (μm)	1.585	0.951
Specific surface area S_V (μm^{-1})	1.088 (15.13%)	0.410 (5.64%)
Pore distribution density PDD (−)	1.454	0.199
Intrinsic permeability k (m^2)	5.77×10^{-17}	1.04×10^{-19}

Note: The numbers indicated in brackets are coefficients of variation for the measured parameters.

stereological terms, and can be derived from the total perimeter length of pore features per unit test area on a statistical basis [21]. This parameter was measured for all the plain mortar specimens in this study.

Another characterizing parameter, the so called pore distribution density (PDD) was also measured for the two groups of plain mortar samples. The pore distribution density is a three-dimensional structural parameter derived from the skeleton length of pore features observed on two-dimensional section images. For details of the definition and measurement procedures of this parameter, see Hu [22]. This parameter has been found to show a high degree of correlation with water permeability of cement pastes than the conventional parameters of porosity and critical pore size often used for characterizing the pore structure [22]. The good correlation can be attributed to the fact that this new parameter PDD contains information on both pore size and connectivity of pore space. Results of the pore structure analysis are summarized in Table 3 for the plain mortars. The derived structural information allows prediction of the intrinsic permeability, k of the mortars on the basis of empirical relationships between pore structure and permeability. For this purpose, an upgraded version of the Katz–Thompson equation was employed, which incorporates the PDD and has been demonstrated to be capable of significantly improving the quality of predicted values [22]. Calculated values of permeability are also given in Table 3. Results reveal clearly that permeability of the mortars decreased by two orders of magnitude for the specimens prepared using admixed chlorides. The estimation is generally in line with the experimental measurements of Loosveldt et al. [23] under comparable conditions. These results confirm the close relationship between pore structure and permeability of cementitious materials.

As discussed in Section 3.1, the similar resistivity measurement results, given in Fig. 2 for the two groups of plain mortars, imply that pore solution chemistry is not the only decisive factor affecting the resistivity of mortars and concretes, but a combined effect of ion transport mechanisms and the resulting alterations in the pore structure are inducing the development of the electrical properties. Polder and Peelen [24] showed the existence of a linear relationship between the diffusion chloride coefficient, D_{Cl} and inverse of resistivity, $1/\rho$ which is the conductivity. Although the diffusion of chloride ions into mortars and concretes is known to contribute to the overall electrical properties, the relationship between chloride concentration and electrical resistivity is apparently not always linear i.e. increased resistivity does not always mean lowering chloride concentration. The factor which influences the electrical resistivity in cement-based materials at most, is the moisture content. When chlorides are present in the bulk mortar or concrete matrix, significantly contributing factors become the chemical binding mechanisms and microstructural properties. The former contribute to morphological alterations in hydration products and surface charge of the bulk matrix i.e. the influence of the pore solution ions can be quite significant. The latter determine the electrolytic path in the system and the pore interconnectivity i.e. the ease of aggressive ion penetration and further ion transport.

Table 4
Corrosion current and corrosion rate for the reinforced mortars (w/c ratio 0.6, 65 and 120 days)

Hydration time	Reinforced mortars	Potential E_{corr} (mV SCE)	Corrosion current I_{corr} (μA/cm^2)	Corrosion rate (μm/year)
65 days	Corroding N	−528	0.39	4.52
	Reference R	−349	0.09	1.04
120 days	Corroding N	−678	0.79	9.16
	Reference R	−450	0.14	1.62

TN specimens were used to determine the coefficient of chloride diffusion, D_{Cl} in the plain mortars. One longitudinal half of specimens were mixed using tap water, while the other half was mixed using NaCl solution. This arrangement sets up a chloride concentration gradient between the two halves of the same mortar specimen (see Table 1). Since a non-steady state condition is applicable here, the second Fick's law was used $\partial c/\partial t = \partial/\partial x(D(\partial c/\partial x))$, where D is the diffusion coefficient. The Crank's solution to this equation was used for estimating, D_{Cl}. The Crank's solution is given as $c = c_0[1-\text{erf}(x/2\sqrt{Dt})]$, where c is the chloride concentration at distance x (kg/m^3), c_0 is the chloride concentration at the exposed surface (kg/m^3) (in this case c_0 is the concentration in section B2 in specimens TN, Table 1), x is the distance from the exposed surface. The values of $\text{erf}(x/2\sqrt{Dt})$ vs $x/2\sqrt{Dt}$ are available in standard tables.

Based on the chloride profiles obtained along the longitudinal direction of TN specimens, D_{Cl} was calculated to be 6.5×10^{-10} m^2/s in the plain mortars, which is higher compared to the values of 0.4×10^{-12} to 1×10^{-12} reported by Gaal [25] for cement-based materials using the same type of cement and w/c ratios. Along with the high chloride concentrations, in the range of 0.73% to 0.93% per mass of binder, in the separate sections of specimens TN (reported threshold values are varying from 0.2 to 2 wt.% per mass of binder [25]), the group of plain mortar prisms would have been a highly corrosive environment if reinforcement was present in the prisms. Hence, in terms of corrosion risks, the similar electrical resistivity values in specimens T (no chlorides) and specimens N and TN (with admixed chlorides) would not mean low corrosion risk in the latter two groups.

4.2. Electrical resistivity of reinforced mortars

Electrical resistivity of reinforced mortar specimens was estimated by means of EIS measurements (experimental conditions and set-up as in Table 1, points 1,3). The high frequency arcs of the Nyquist plots represent the electrolyte resistance. In the present study, the term 'electrolyte resistance' includes the mortar resistance. The equivalent electrical circuits used to calculate and interpret results represent a series of capacitors and resistances. The calculation gave an electrical resistivity of 40 Ω m for the corroding samples N, and a value of 120 Ω m for the reference sample R, both at 120 days of cement hydration. The finer pore network (lower porosity and reduced critical pore size) in the corroding specimens, denoted to accelerated hydration in the presence of NaCl (Section 3.3, Figs. 11 and 12) and relevant microstructural alterations in the bulk matrix, will certainly contribute to the corrosion process in terms of lowering the rate of

further chloride ingress. The denser pore structure of specimens N however is counterbalanced by the percolating network of interconnected (through voids and pores) cracks, appearing as result of volume expansion of corrosion products. Hence, the electrical resistivity in specimens N is significantly lower, despite the lower porosity (Fig. 12) compared to specimens R. The relatively high resistivity for reference sample R could be partly attributed to the absence of chlorides in the mortar.

4.3. Corrosion rate and resistance

Corrosion current and corrosion rate are usually calculated on the basis of polarization resistance obtained by the LPR method. The values of R_p calculated by LPR and EIS are generally in agreement with each other [26]. The relationship between R_p and I_{corr} is given by $R_p = \Delta E / I$. The applied potential is plotted versus the measured current, then the R_p obtained is used to calculate the steel corrosion current density according to Stern–Geary formula $I_{corr} = B / R_p$, where B is $\beta_a \beta_c / 2.30 (\beta_a + \beta_c)$, β_a and β_c are the cathodic and anodic Tafel constants in mV/decade. In this study, $B = 26$ mV was used for the corroding specimens and $B = 52$ mV was used for the reference samples considered to be in passive condition [27]. In general, the corrosion rate is proportional to the corrosion current density, and the latter is inversely proportional to R_p. When plotting corrosion current versus resistivity on a semi-log scheme, a negative linear relationship exists. Since the parameters discussed are commonly related, the corrosion condition can be evaluated by some or any of them.

Table 4 gives results of the potentials measured, the calculated corrosion currents and the corrosion rates for reinforced mortars after 65 and 120 days of hydration. The corrosion potentials were found to be consistent with the experimental data reported in literature for cement mortars [24]. Andrade et al. [27] assumed a value of 1 μm/year for the threshold corrosion rate between passive and active corrosion state of the steel bar reinforcement. Hence, the samples N can be classified as actively corroding, with corrosion rates close to or exceeding 10 μm/year at 120 days of cement hydration.

5. Conclusions

This contribution to research was focussed on microstructural analysis and measurement of electrochemical characteristics and electrical and microstructural properties of plain and reinforced mortars in the presence of chlorides. Admixed chloride ions were found to induce changes in chemical compositions of hydration products resulting in the formation of C–S–H with a high Ca/Si ratio in the range of 2.19 to 2.95. The corrosion products observed mainly consisted of iron oxides and iron oxychloride complexes of different compositions and morphological features. Use of quantitative pore structure characteristics of mortars, determined from SEM micrographs with the support of image analysis software has been explored in relation to durability-related physical properties of mortars.

Mortars with and without admixed chlorides gave similar electrical resistivity values at early ages. It is likely that the pore refining effect of accelerated hydration due to admixed chlorides

in the plain mortars (consequently pore network structural changes) are affecting the electrical properties at most, which is in addition to the physico-chemical alterations in the C–S–H matrix.

Evidenced by the microstructural analysis of the reinforced mortar cylinders, chloride ingress exerts similar effects of pore refinement, but electrical properties here are determined by a combined influence of chloride binding mechanisms and corrosion process i.e. the denser pore structure of the bulk matrix in corroding specimens is counterbalanced by the percolating network of interconnected cracks (appearing as result of volume expansion of corrosion products).

Hence, electrical resistivity, electrolytic paths and chloride-induced corrosion respectively, are not only dependent on the presence of conductive ions (as chlorides) in the pore solution, but are also a function of the pore structure of the bulk cementitious matrix.

References

[1] F.P. Glasser, Chemistry of alkali-aggregate reaction, in: R.N. Swamy (Ed.), The Alkali-Silica Reaction in Concrete, Van Nostrand Reinhold, New York, 1992, pp. 30–53.

[2] V.S. Ramachandran, Concrete Science, Noyes/William Andrew, Norwich, 2001 Ch.7.

[3] P. Shiessl, Corrosion of steel in concrete, Report of Technical Committee, RILEM, 1988.

[4] G.K. Glass, N.R. Buenfeld, The presentation of the chloride threshold level for corrosion of steel in concrete, Corrosion Science 39 (1997) 1001–1013.

[5] D.A. Koleva, J. Hu, A.L.A. Fraaij, P. Stroeven, Influences of chloride ions on plain and reinforced mortars investigated by combined microstructure and electrochemical approaches, EFC Proceedings, event n:273: EUROCORR 2005, Lisboa, Portugal, paper No.315.

[6] V. Feliú, J.A. González, C. Andrade, S. Feliú, Equivalent circuit for modelling the steel-concrete interface. I. Experimental evidence and theoretical predictions, Corrosion Science 40 (1998) 975–993.

[7] C. Andrade, L. Soler, C. Alonso, R.X. Nóvoa, M. Keddam, The importance of geometrical considerations in the measurement of steel corrosion in concrete by means of AC impedance, Corrosion Science 37 (1995) 2013–2023.

[8] O. Poupard, A. Aït-Mokhtar, P. Dumargue, Corrosion by chlorides in reinforced concrete: determination of chloride concentration threshold by impedance spectroscopy, Cement and Concrete Research 34 (2004) 991–1000.

[9] J. Hu, P. Stroeven, Application of image analysis to assessing critical pore size for permeability prediction on cement paste, Image Analysis and Stereology 22/2 (2003) 97–103.

[10] K.L. Scrivener, Backscattered electron imaging of cementitious microstructures: understanding and quantification, Cement and Concrete Composites 26 (2004) 935–945.

[11] J. Serra, Image Analysis and Mathematical Morphology, Academic Press, London, 1982.

[12] A.J. Katz, A.H. Thompson, Quantitative prediction of permeability in porous rock, Physics Review B 34/11 (1986) 8179–8181.

[13] P.J.M. Monteiro, K. Wang, G. Sposito, M.C. dos Santos, W.P. de Andradef, Influence of mineral admixtures on the alkali-aggregate reaction, Cement and Concrete Research 27 (1997) 1899–1909.

[14] F. Pruckner, O.E. Gjörv, Effect of CaCl$_2$ and NaCl additions on concrete corrosivity, Cement and Concrete Research 34 (2004) 1209–1217.

[15] M.N. Haque, O.A. Kayyali, Free and water soluble chloride in concrete, Cement and Concrete Research 25 (1995) 531–542.

[16] W.J. McCarter, G. Starrs, T.M. Chrisp, Electrical conductivity, diffusion and permeability of Portland cement-based mortars, Cement and Concrete Research 30 (2000) 1395–1400.

[17] A.D. Buck, A discussion of the paper, 'The penetration of chlorides into hardened cement pastes' by H.D. Midgley and J.M. Illston, Cement and Concrete Research 15 (1985) 933–934.

[18] M.F. Montemor, A.M.P. Simoes, M.G.S. Ferreira, Chloride-induced corrosion: fundamental and techniques, Cement and Concrete Composites 25 (2003) 491–502.

[19] A.K. Suryavanshi, J.D. Scantlebury, S.B. Lyon, Pore size distribution of OPC and SRPC mortars in presence of chlorides, Cement and Concrete Research 25 (1995) 980–988.

[20] B. Díaz, X.R. Nóvoa, M.C. Pérez, Study of the chloride diffusion in mortar: a new method of determining diffusion coefficients based on impedance measurements, Cement and Concrete Composites 28 (2006) 237–245.

[21] E.E. Underwood, Quantitative Stereology, Addison-Wesley Publishing Company, Reading (MA), 1968.

[22] J. Hu, Porosity of Concrete — Morphological Study of Model Concrete, PhD thesis, Delft University of Technology, Rotterdam: OPTIMA Grafische Communicatie, 2004.

[23] H. Loosveldt, Z. Lafhaj, F. Skoczylas, Experimental study of gas and liquid permeability of a mortar, Cement and Concrete Research 32 (2002) 1357–1363.

[24] R.B. Polder, W.H.A. Peelen, Characterisation of chloride transport and reinforcement corrosion in concrete under cyclic wetting and drying by electrical resistivity, Cement and Concrete Composites 24 (2002) 427–435.

[25] G. Gaal, Prediction of deterioration of concrete bridges, PhD thesis, Delft University of Technology. Delft University Press, 2004.

[26] D.A. Koleva, A.L.A. Fraaij, J. Hu, N. Boshkov, Steel corrosion in mortar specimens deteriorated by chloride ingress: electrochemical study using AC and DC methods, 207th Meeting of the Electrochemical Society, Quebec, Canada, 2005.

[27] C. Andrade, V. Castelo, C. Alonso, J.A. Gonzales, Determination of the Corrosion Rate of Steel Embedded in Concrete, STP, vol. 906, ASTM Special Technical Publication, Philadelphia, 1986, p. 43.